ELSEVIER

Journal of Nuclear Materials 256 (1998) 35–46

journal of nuclear materials

Modelling of the mechanical behavior of the metal–oxide system during Zr alloy oxidation

M. Parise [a,b], O. Sicardy [b], G. Cailletaud [a,*]

[a] *Centre des matériaux Pierre-Marie Fourt, Ecole Nationale Supérieure des Mines de Paris, CNRS URA 866, B.P. 87, F-91003 Evry cedex, France*

[b] *CEA-CEREM, DEM/SPCM, CEA-Grenoble, 17, rue des Martyrs, 38054 Grenoble cedex 9, France*

Received 24 November 1997; accepted 2 March 1998

Abstract

During the oxidation of Zircaloy fuel cladding, large stresses develop in the oxide layer. This paper presents two approaches to evaluate the stresses in the metal, modelled as a viscoplastic material, and the oxide, considered as elastic transverse isotropic. The first approach is a computation of the stresses in the whole cladding on a 1D radial geometry. It evidences large compressive hoop stresses in the oxide and weak tensile stresses in the metal. The second approach is a 2D finite elements computation accounting for the undulation of the metal–oxide interface. This specific geometry is found to have an important influence on the local stress state. In particular, radial stresses are evidenced near the metal–oxide interface, whose sign and value depend on the local curvature of the interface.

1. Introduction

Zirconium alloys are used as cladding materials for nuclear fuel in pressurized water reactors (PWR). In the conditions of use (water at 350°C and 150 bars), they oxidize outside into zirconia. Without irradiation, the growth kinetics presents two main steps. At the beginning, the oxide thickness grows as the cube root of time, until it reaches about 2.5 μm, depending on the alloys and the conditions of oxidation. A second step arises then, during which the growth is approximately linear. This transition is likely related to the development of high residual stresses and to the appearance of cracks in the oxide layer. This phenomenon has been described as the 'breakaway oxidation' by Bradhurst and Heuer [1].

The oxide growth occurs at the metal–oxide interface after the inward diffusion of oxygen. The transformation from metal to oxide produces a dramatic volume change, since the volume dilatation equals 1.56 [2], leading to residual stresses in both the layer and the metal. These stresses are responsible for the spalling of the thick layers, they have an effect on the whole deformation of the metal [3], they could favour the stabilisation of the different crystallographic phases of zirconia [4]. They lead to the breakaway transition and they also induce changes in the initial kinetics through the modification of the diffusion coefficient in the oxide [5,6].

The study of the stress level in the zirconium oxide scales appears therefore to be of great importance. It has been indirectly studied through measurements by several methods such as curvature and flexion [1,7,8], or X-rays diffraction [9]. The main difficulty is the lack of knowledge concerning material behaviour. Anyway, these methods give an evaluation of the mean stress value.

In the present paper, the behaviours of the metal and the oxide are specified. Two types of computations are then described. They both aim at computing the stresses and strains in the metal and the oxide during the scale growth. The possibility of the appearance of cracks parallel to the metal–oxide interface in the oxide is studied in relation with the stress state.

* Corresponding author. Tel.: +33-1 60 76 30 56; fax: +33-1 60 76 31 50.

0022-3115/98/$19.00
PII: S0022-3115(98)00045-2

2. Material behaviour

2.1. Metal

The anisotropy of the base metal is quite low. It will then be modelled as an isotropic elasto-viscoplastic material. A von Mises invariant is used to define the yield function f, which involves both linear and non-linear kinematic hardening [10].

The model is summarized by Eqs. (1)–(4), which successively define:

- the strain partition into an elastic and a viscoplastic part (Eq. (1)),
- the yield function (Eq. (2)), in which the superscript d denotes the deviatoric part,
- the definition of the kinematic hardening variable (Eq. (3)),
- the evolution laws for both viscoplastic flow and state variable (Eq. (4)).

$$\underset{\sim}{\varepsilon} = \underset{\sim}{\varepsilon}^{e} + \underset{\sim}{\varepsilon}^{v}, \tag{1}$$

$$f\left(\underset{\sim}{\sigma}, \underset{\sim}{\mathbf{X}}\right) = J\left(\underset{\sim}{\sigma} - \underset{\sim}{\mathbf{X}}\right) - R_0,$$

$$\text{with } J\left(\underset{\sim}{\sigma} - \underset{\sim}{\mathbf{X}}\right) = \sqrt{\frac{3}{2}\left(\underset{\sim}{\sigma} - \underset{\sim}{\mathbf{X}}\right)^{\mathrm{d}} : \left(\underset{\sim}{\sigma} - \underset{\sim}{\mathbf{X}}\right)^{\mathrm{d}}}, \tag{2}$$

$$\underset{\sim}{\mathbf{X}} = \frac{2}{3} C_1 \underset{\sim}{\alpha} + \frac{2}{3} C_2 \underset{\sim}{\varepsilon}^{v}, \tag{3}$$

$$\dot{\underset{\sim}{\varepsilon}}^{v} = \underset{\sim}{\mathbf{n}} \dot{v}, \quad \dot{\underset{\sim}{\alpha}} = \left(\underset{\sim}{\mathbf{n}} - D_1 \underset{\sim}{\alpha}\right) \dot{v},$$

$$\text{with } \dot{v} = \left\langle f\left(\underset{\sim}{\sigma}, \underset{\sim}{\mathbf{X}}\right)/K \right\rangle^{n}, \quad \underset{\sim}{\mathbf{n}} = \frac{\partial f}{\partial \underset{\sim}{\sigma}}. \tag{4}$$

Six temperature-dependent material coefficients have then to be identified, C_1, C_2, D_1, for characterizing kinematic hardening, R_0 as initial threshold, K and n for the rate sensitivity. The values were defined using an identification code [11], using an experimental data base from the literature [12]. They are shown in Table 1, together with the elastic coefficients.

2.2. Oxide

The elastic constants of a monocrystal of monoclinic zirconia show the large anisotropy of the material [13]. In the crystallophysic reference frame (see Fig. 1), the compliance tensor reads

Table 1
Values at 350°C of the viscoplastic law parameters

E (GPa)	v	R_0 (MPa)	C_1 (MPa)	C_2 (MPa)	D_1 (MPa)	K (MPa $s^{1/n}$)	n
80	0.3	36.5	22 000	1400	560	380	4.3

$$\underset{\approx}{\mathbf{S}}(\mathrm{GPa}^{-1}) = \begin{bmatrix} 0.00345 & -0.00128 & -0.00116 & 0 & 0.00173 & 0 \\ -0.00128 & 0.00355 & -0.00178 & 0 & -0.00268 & 0 \\ -0.00116 & -0.00178 & 0.00537 & 0 & 0.00242 & 0 \\ 0 & 0 & 0 & 0.0114 & 0 & 0.00342 \\ 0.00173 & -0.00268 & 0.00242 & 0 & 0.00153 & 0 \\ 0 & 0 & 0 & 0.00342 & 0 & 0.00873 \end{bmatrix}. \tag{5}$$

The values of the Young modulus and Poisson's ratio can be computed for various crystallographic directions. The extreme values for any direction of the crystallophysic space are 144 GPa and 324 GPa for the apparent Young modulus and 0.13 and 0.43 for the apparent Poisson's ratio.

In the oxide layers grown on the zirconium alloys for cladding materials, a fibre texture has been evidenced [14,15]. The axis of the fibre texture, i.e. the crystallographic direction common to a large majority of the grains of the oxide, is close to the c axis of the unit cell (see Fig. 1). The study of the texture shows that as a first approach, the grains are free to rotate around this direction. The resulting material has then five coefficients, due to the transverse isotropy around the fibre axis. The compliance tensor is then

$$\underset{\approx}{\mathbf{S}}\ (\mathrm{GPa}^{-1}) = \begin{bmatrix} S_{11} & S_{12} & S_{13} & 0 & 0 & 0 \\ S_{12} & S_{22} & S_{13} & 0 & 0 & 0 \\ S_{13} & S_{13} & S_{33} & 0 & 0 & 0 \\ 0 & 0 & 0 & S_{44} & 0 & 0 \\ 0 & 0 & 0 & 0 & S_{44} & 0 \\ 0 & 0 & 0 & 0 & 0 & 2(S_{11} - S_{12}) \end{bmatrix}. \tag{6}$$

The values of S_{ij} are computed in Appendix A.

2.3. Volumic dilatation

Pilling and Bedworth have computed the volumic dilatation associated with the oxidation of numerous metals [2]. This ratio equals 1.56 for Zr/ZrO_2 system. Bradhurst and Heuer have calculated the stresses induced by the oxidation in oxide layers grown on Zircaloy-2, when measuring strains by the curvature method [1]. Using the Pilling and Bedworth ratio, and assuming isotropic distribution of the dilatation, they obtain growth stresses near 33 GPa, which cannot be considered as a reasonable level in the oxide layer. More recently, Bernstein attempted to compensate this by modifying the dilatation by a coefficient smaller than 1, to be adjusted for each metal–oxide system and geometry [3]. The physical basis for such a modification is not clear and it seems more pertinent to reconsider the assumption of isotropy.

In the following we consider that the volumic dilatation is represented by an anisotropic strain tensor, ε^{pt}.

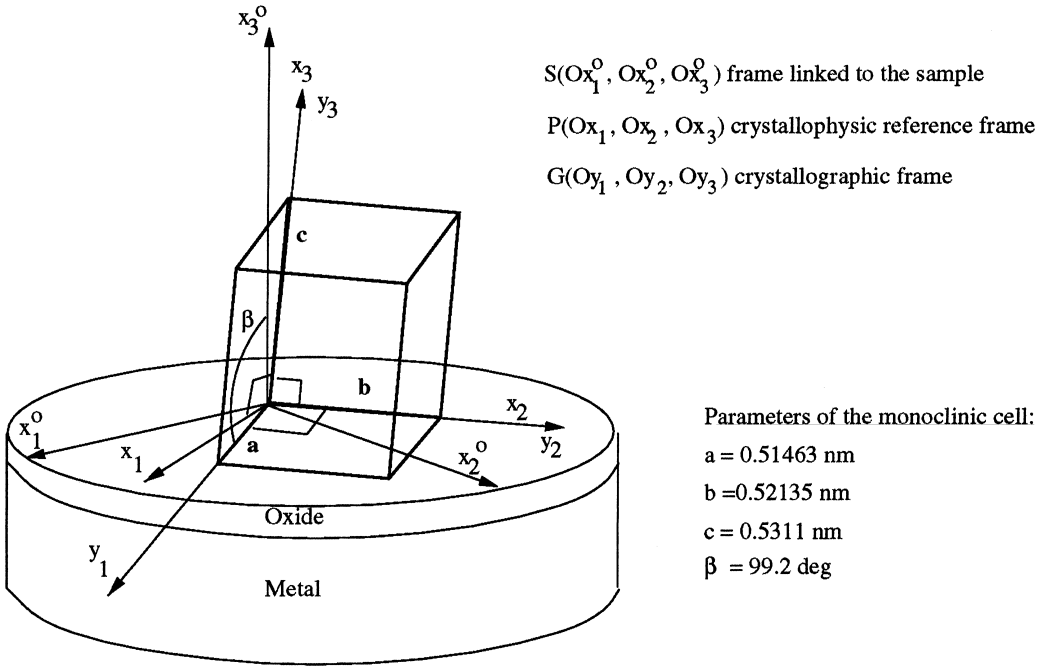

Fig. 1. Definition of the reference crystallophysic frame.

This tensor is assumed to be diagonal if expressed in the S frame (frame linked to the sample, see Fig. 1) and the dilatation is isotropic in the plane corresponding to the metal–oxide interface.

$$\underset{\sim}{\varepsilon}^{pt} = \begin{bmatrix} \varepsilon_1^{pt} & 0 & 0 \\ 0 & \varepsilon_1^{pt} & 0 \\ 0 & 0 & \varepsilon_3^{pt} \end{bmatrix}, \tag{7}$$

where ε_1^{pt} and ε_3^{pt} are linked together to give the Pilling and Bedworth ratio.

The value of ε_1^{pt} has been identified in the case of the Zircaloy-4/ZrO_2 system by modelling deflection experiments from the literature [8]. The samples are narrow sheets of Zircaloy-4, 45 mm long, 0.4 mm thick and 5 mm wide, protected against oxidation on one side. They are oxidized in oxygen at 450°C. Growth stresses in the oxide layer induce a deflection of the blade, which can be measured in situ through a quartz window of the furnace.

The computation is achieved within the generalized plane strain hypothesis, since the deflection around the y axis (see Fig. 2) is the only one to be considered. As shown in Fig. 2, the specimen is divided into 20 × 20 elements (15 in the metal and 5 in the oxide), with a geometrical progression near the metal–oxide interface. The size of the first element near the interface is then about 200 nm. Three different meshes are submitted to the computation to represent different oxide thicknesses. For each oxide thickness, the computation is performed with seven values for ε_1^{pt}, from 0.001 to 0.010. The volumic expansion is modelled as a pseudo-thermal dilatation. ε_1^{pt} is modelled as $\alpha_1 T$, with $T = 1$ and α_1 taking the proper values. The boundary conditions prescribed are null vertical and horizontal displacements at the left of the structure. The behaviours of metal and oxide are

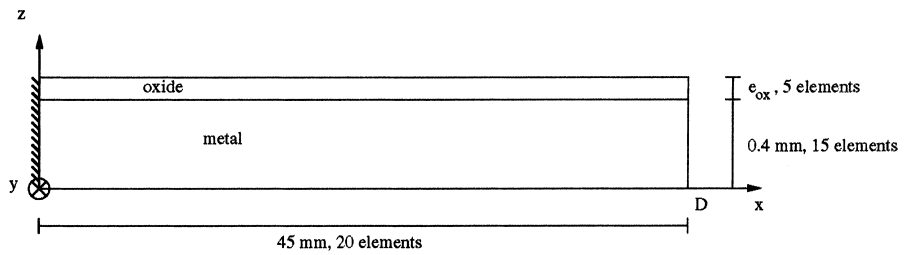

Fig. 2. Geometry of the specimen for the deflection experiment [8].

modelled as previously (see Sections 2.1 and 2.2). The deflection values (vertical displacement of point D) computed for each oxide thickness e_{ox} and ε_1^{pt} are summarized in Table 2.

The deflection versus oxide thickness curves are presented in Fig. 3. The deformed structure after computation is presented in Fig. 4. The comparison with experimental results from Ref. [8] shows that the optimal value for ε_1^{pt} is 0.005, leading to the expansion strain tensor

$$\underset{\sim}{\varepsilon}^{pt} = \begin{bmatrix} 0.005 & 0 & 0 \\ 0 & 0.005 & 0 \\ 0 & 0 & 0.54 \end{bmatrix}. \quad (8)$$

The former values in the phase transformation tensor have to be considered only as a good order of magnitude. In fact, two points have to be specified for a more precise modelling of the deflection experiments. First, the elastic constants for ZrO_2 are unknown at 450°C so that room temperature constants were used. Second, even though the length of the samples is known to be 45 mm, nothing is specified in Ref. [8] about the true free length of the sample submitted to the deflection.

Table 2
Different values for ε_1^{pt} tested in the deflection modelling

ε_1^{pt}	0.001	0.005	0.010
Deflection (mm) for $e_{ox} = 3$ μm	0.38	1.92	3.04

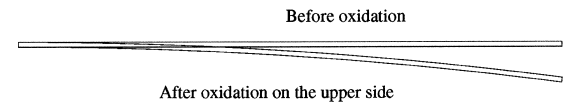

Fig. 4. Computed deflected blade for $\varepsilon_1^{pt} = 0.005$ and an oxide thickness $e = 3$ μm.

3. Global modelling

In this first approach, the interface is supposed to be a circle in a plane perpendicular to the axis of the tube. The geometry of the problem is then axisymmetric. This system is classically used by the authors for the study of the metal–oxide system. In this case, the problem can be solved through a semi-analytical analysis. First, the system of equations is written (momentum conservation, compatibility and boundary conditions), then the expressions are implemented in a numerical program giving the solution of the problem along the radius of the tube.

3.1. Formulation of the analytical problem

The geometry of the system is defined in Fig. 5. It is assumed that the tube is long. As the symmetry axes of the material are r, θ, z, these directions correspond to the principal directions for both stress and strain. The only nonzero component of the displacement is the radial one and the only nonzero component of stresses and strains are respectively $\sigma_r, \sigma_\theta, \sigma_z$ and $\varepsilon_r, \varepsilon_\theta, \varepsilon_z$. The previous variables only depend on r. The metal (Zircaloy-4) has an

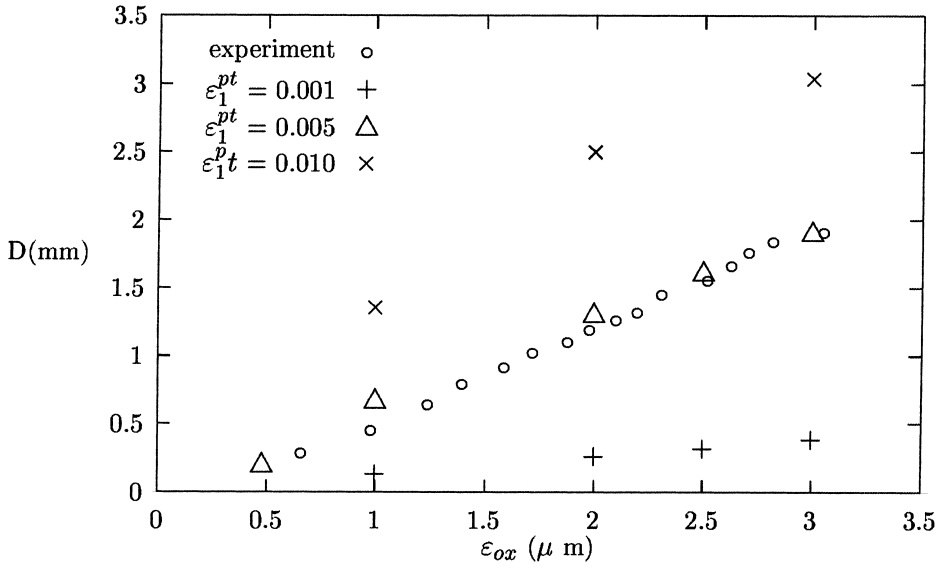

Fig. 3. Comparison between modelled deflection curves and experimental results.

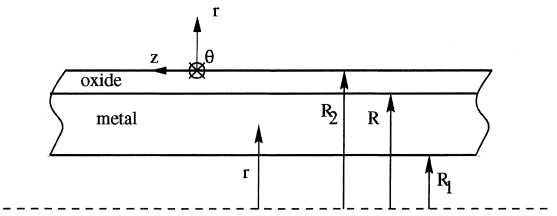

Fig. 5. Geometry and notation of the axes in the global model.

elasto-viscoplastic behaviour. The total tensor reads then

$$\underset{\sim}{\varepsilon} = \underset{\sim}{\varepsilon}^{e} + \underset{\sim}{\varepsilon}^{v}. \tag{9}$$

There are thus nine unknowns in the metal: $\sigma_r, \sigma_\theta, \sigma_z, \varepsilon^e_r, \varepsilon^e_\theta, \varepsilon^e_z, \varepsilon^v_r, \varepsilon^v_\theta$ and ε^v_z. The oxide has an elastic behaviour and undergoes the phase transformation strain previously identified. The total strain tensor in the oxide reads then

$$\underset{\sim}{\varepsilon} = \underset{\sim}{\varepsilon}^{e} + \underset{\sim}{\varepsilon}^{pt}. \tag{10}$$

There are thus six variables in the oxide: $\sigma_r, \sigma_\theta, \sigma_z, \varepsilon^e_r, \varepsilon^e_\theta$ and ε^e_z. In both materials, the stresses and the elastic strains are linked through the Hooke's law. In the metal, E being the Young modulus and v the Poisson's ratio, the equation reads

$$\begin{pmatrix} \varepsilon^e_r \\ \varepsilon^e_\theta \\ \varepsilon^e_z \end{pmatrix} = \frac{1}{E} \begin{pmatrix} 1 & -v & -v \\ -v & 1 & -v \\ -v & -v & 1 \end{pmatrix} \begin{pmatrix} \sigma_r \\ \sigma_\theta \\ \sigma_z \end{pmatrix}. \tag{11}$$

The viscoplastic relations give three more equations. In the oxide, S_{ij} being the compliances, Hooke's law reads, in (θ, z, r) frame,

$$\begin{pmatrix} \varepsilon^e_r \\ \varepsilon^e_\theta \\ \varepsilon^e_z \end{pmatrix} = \begin{pmatrix} S_{11} & S_{12} & S_{12} \\ S_{12} & S_{22} & S_{23} \\ S_{12} & S_{23} & S_{22} \end{pmatrix} \begin{pmatrix} \sigma_r \\ \sigma_\theta \\ \sigma_z \end{pmatrix}. \tag{12}$$

There are now six equations in the metal and three in the oxide. The equilibrium, compatibility and boundary conditions will provide the three missing equations. In the present case, these three equations reduce to

$$\sigma_r - \sigma_\theta + r\sigma_{r,r} = 0, \tag{13}$$

$$\varepsilon_r = (r\varepsilon_\theta)_{,r}, \tag{14}$$

$$\varepsilon_z = \varepsilon_0, \tag{15}$$

where ε_0 is a constant, independent of r, determined by the generalized plane strain condition.

The systems composed of Eqs. (9), (11), (13)–(15) and Eqs. (10), (12)–(15) can be solved in the metal and the oxide, respectively. The expressions of the stresses are given by Eqs. (16) and (17), respectively:

$$\begin{aligned} \sigma_r(r) &= \frac{M}{2}\left(1 - \frac{R_1^2}{r^2}\right) + g(r), \\ \sigma_\theta(r) &= \frac{M}{2}\left(1 + \frac{R_1^2}{r^2}\right) + rg'(r) + g(r), \\ \sigma_z(r) &= v(\sigma_r + \sigma_\theta)(r) + E\left(\varepsilon_0 - \varepsilon^v_z(r)\right), \end{aligned} \tag{16}$$

with

$$\begin{aligned} g(r) = \frac{E}{2(1-v^2)} \Bigg[\int_{R_1}^{r} \Bigg(& \frac{(\varepsilon^v_r - \varepsilon^v_\theta)(x)}{x} \\ & - \frac{x(\varepsilon^v_r + \varepsilon^v_\theta + 2v\varepsilon^v_z)(x)}{r^2} \Bigg) \, \mathrm{d}x + (\varepsilon^v_\theta \\ & + v\varepsilon^v_x)(R_1)\left(1 - \frac{R_1^2}{r^2}\right) \Bigg], \end{aligned}$$

$$\begin{aligned} g'(r) = \frac{E}{r^3(1-v^2)} \Bigg[& \int_{R_1}^{r} x(\varepsilon^v_r + \varepsilon^v_\theta + 2v\varepsilon^v_z)(x) \, \mathrm{d}x \\ & + R_1^2(\varepsilon^v_\theta + v\varepsilon^v_z)(R_1) - r^2(\varepsilon^v_\theta + v\varepsilon^v_z)(r) \Bigg], \end{aligned}$$

$$\begin{aligned} \sigma_r(r) &= Nr^{\lambda-1} - (NR_2^{\lambda-1} + K + L\varepsilon_0)\left(\frac{R_2}{r}\right)^{\lambda+1} + K + L\varepsilon_0, \\ \sigma_\theta(r) &= \lambda Nr^{\lambda-1} + \lambda(NR_2^{\lambda-1} + K + L\varepsilon_0)\left(\frac{R_2}{r}\right)^{\lambda+1} \\ &\quad + K + L\varepsilon_0, \\ \sigma_z(r) &= \frac{\varepsilon_0 - \varepsilon^{pt}_z}{S_{22}} - \frac{S_{12}\sigma_r(r) + S_{23}\sigma_\theta(r)}{S_{22}}, \end{aligned} \tag{17}$$

with

$$\lambda = \sqrt{\frac{S_{11}S_{22} - S_{12}^2}{S_{22}^2 - S_{23}^2}},$$

$$L = \frac{S_{12} - S_{23}}{S_{22}^2 - S_{23}^2}\frac{1}{1-\lambda^2},$$

$$K = \left(\frac{\varepsilon^{pt}_r - \varepsilon^{pt}_\theta}{S_{12} - S_{23}}S_{22} - \varepsilon^{pt}_z\right)L,$$

where M, N are integration constants. M, N and ε_0 are determined with additional boundary conditions:

- continuity of the radial stress at the metal–oxide interface, $\sigma_r^{\mathrm{Zr}}(R) = \sigma_r^{\mathrm{ZrO_2}}(R)$,
- continuity of the hoop strain at the metal–oxide interface, $\varepsilon_\theta^{\mathrm{Zr}}(R) = \varepsilon_\theta^{\mathrm{ZrO_2}}(R)$,

- no axial force applies at the end of the tube, $2\pi \int_{R_1}^{R_2} r\sigma_z(r)\ \mathrm{d}r = 0$.

The problem is solved numerically, after a discretization of the r axis. At the beginning of the computation, the structure is fully metallic. The law describing the growth of the oxide scale results from a previous study of the oxidation kinetics of Zircaloy-4 in water, at 340°C, 15 MPa [14]. The best agreement between the law and the experimental thickness versus time curve was achieved with Eq. (18):

$$e = (50^{2.85} + 190\,000t)^{1/2.85}, \quad e \text{ in nm and } t \text{ in h.} \qquad (18)$$

These kinetics are prescribed as an input to the code. At each step, Eqs. (16) and (17) are computed by the program and, if needed, the viscoplastic equations are integrated. The computation is stopped when the oxide thickness reaches 2.5 μm (mean kinetics transition thickness).

3.2. Results

One hundred fifteen elements were used in the computation. The stress variation according to the radius in the cladding, in both metal and oxide, are presented in Fig. 6. The radial stress is continuous through the metal–oxide interface, its value remains very low (about 1 MPa). The hoop and axial stresses are discontinuous through the interface. Large compressive stresses are observed in the oxide (about 2 GPa), due to the nearly null displacement in hoop direction and to the important phase transformation strain. These results are consistent with experimental results concerning oxide layers grown on the same materials [9]. Due to the low equivalent stresses observed in the metal (about 10 MPa), the substrate remains elastic.

Note that thermal stresses resulting from cooling are negligible in comparison with the growth stresses computed here. Assuming an oxide thickness $e_{ox} = 2$ μm, a Young modulus $E_{ox} = 200$ GPa, thermal linear dilatation coefficients for metal $\alpha_m = 5.8 \times 10^{-6}\ K^{-1}$ and for oxide $\alpha_{ox} = 8 \times 10^{-6}\ K^{-1}$, thermal stresses are, in the case of our geometry: $\sigma_r^{th} = 0.04$ MPa and $\sigma_\theta^{th} = 160$ MPa.

The first computation allows us to recover realistic stress level, but it does not give the keys for explaining the presence of cracks parallel to the interface. The radial stress is only due to the curvature of the cladding and would disappear for the case of a plane interface. An alternative approach, used in the next modelling, consists then in considering the undulation of the metal–oxide interface experimentally observed (see [14,16]) for performing a more detailed mechanical analysis. We have then to consider the geometry of the metal–oxide interface on a microscopic level for mechanical analysis, as

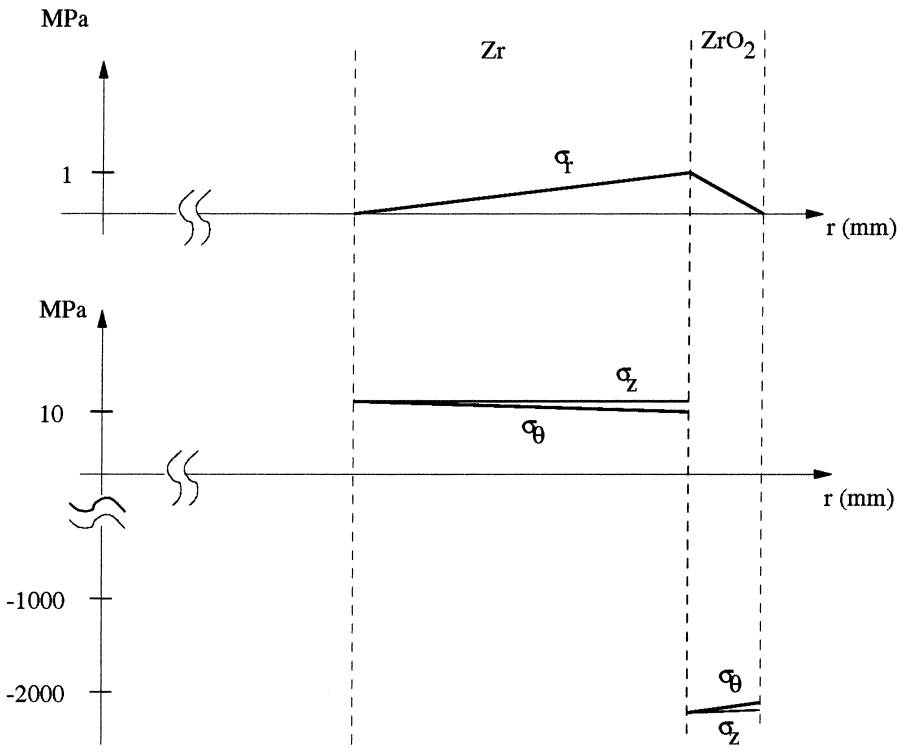

Fig. 6. Stresses in the oxidized cladding computed by the global model.

pointed out by Stott and Atkinson [17]. As shown in the next section, this 'local modelling' will produce the same kind of axial and hoop stresses, but will allow us to explain the presence of a noticeable radial stress.

4. Local modelling

4.1. Basis of the local analysis

In this section the metal–oxide interface is no longer plane but has an undulated geometry. As the undulation does not depend on the direction of the cutting plane perpendicular to the interface, the interface can be considered as having the shape of an 'egg-carton'. The observation of scanning electron microscopy (SEM) photographs have shown that both the period and the amplitude of the undulations evolve during the oxide growth [14]. The following computation tends to exhibit the effect of such an undulation of the interface. For that purpose, we now consider one wavelength, whose geometry is axisymmetric around the radius of the tube.

4.2. Formulation of the problem

The computed structure, shown in Fig. 7, is a cylinder whose radius equals half a period of an undulation. Note that z' corresponds now to the radius of the tube, while r' stands for any direction in the plane tangent to the tube. The cylinder is 5 μm high and the mean position of the metal–oxide interface can vary, the mean oxide thickness ranking from 0.5 to 2 μm. The points of the interface have their z-coordinates defined as follows:

$$z' = z'_{\text{int}} + a \cos\left(\frac{\pi r'}{r'_{\max}}\right),$$

where z'_{int} is the mean interface position, r' the radial position in the cylinder, $r'_{\max}$ the radius of the cylinder and a the amplitude of the undulation. The computation is performed using the finite element code ZEBULON [18]. The structure is divided into 600 elements in the metal (20×30) and 200 in the oxide (20×10), with a geometrical progression near the interface. The size of the elements near the interface is then about 30 nm. The elements used are 8 nodes quadrilateral, with full integration. The boundary conditions are a prescribed null displacement at the bottom of the structure and a prescribed null horizontal displacement at $r' = r'_{\max}$.

The latter condition is used to express that the rest of the base metal, which is not represented in the mesh, forbids any radial displacement. The material behaviour is the same as in the previous section. In order to separately investigate the influence of the oxide thickness and the amplitude of the undulation on the intensity of the stresses, several cases will be considered. First, three different thicknesses e (0.5, 1 and 1.5 μm) are considered with an undulation amplitude of 0.1 μm. Second, three different undulation amplitudes a (0.05, 0.1 and 0.2 μm) are chosen for an oxide thickness of 1 μm. The values of these amplitudes are estimated from SEM photographs. They do not result from a systematic analysis of the interface geometry but are realistic values.

The same kind of computation can be performed with opposite curvature of the interface (i.e. with oxide thickness greater at the center of the structure element cylinder in Fig. 7).

4.3. Results

In the following paragraph, 'radial', 'hoop' and 'axial' will still refer to the directions of the cladding, as in Section 3, in order to allow an easy comparison between global and local calculations.

The distribution of the stresses in the structure is summarized in Fig. 8. First, we can check that far from the metal–oxide interface, the sign and the intensity of

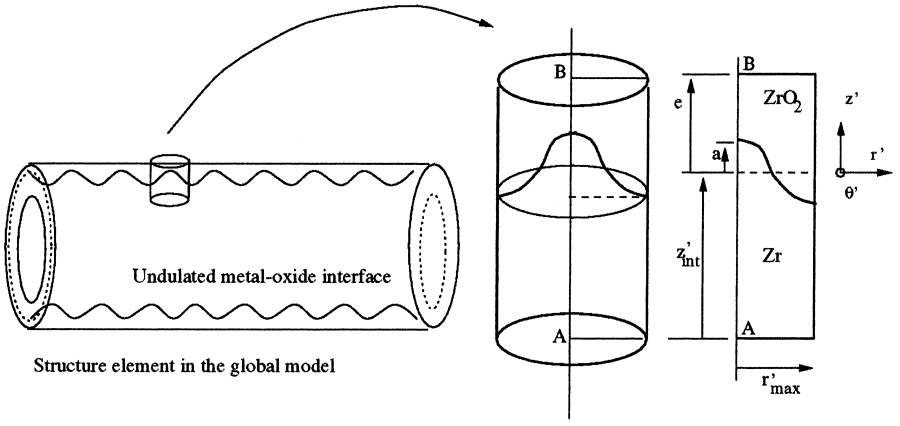

Fig. 7. Structure of the unit cell for local modelling.

the stresses are the same as in the global model. These are compressive hoop stresses in the oxide about 2 GPa, and no radial stresses neither in the metal nor in the oxide. However, the effect of the undulation of the interface clearly appears. The hoop stresses are modified in the vicinity of the interface. In the oxide, the compressive stresses become greater and in the metal tensile stresses arise. The main change concerns the radial stress. Instead of no radial stress in the case of a flat interface in the global model, some tensile stresses are evidenced here because of the local curvature of the interface. As shown in Figs. 9–12, the level of the different stresses only depends on the amplitude of the undulation. Between 0.5 and 2 μm, the oxide thickness has no effect. On the other hand, increasing the amplitude of the undulation produces larger stresses near the interface. The effect of the undulation concerns a volume of matter from a few hundred cubic nanometers to 1 μm around the interface depending on the undulation sharpness. Within this small volume of matter, the metal deforms viscoplastically. Viscoplastic strain reaches 0.18, at approximately 200 nm beneath the interface. The von Mises stress is high and reaches several hundred MPa in the metal beneath the interface. Finally, the general deformation of the structure tends to increase the undulation amplitude.

When the computation is achieved with the opposite curvature of the interface, it appears that the hoop and

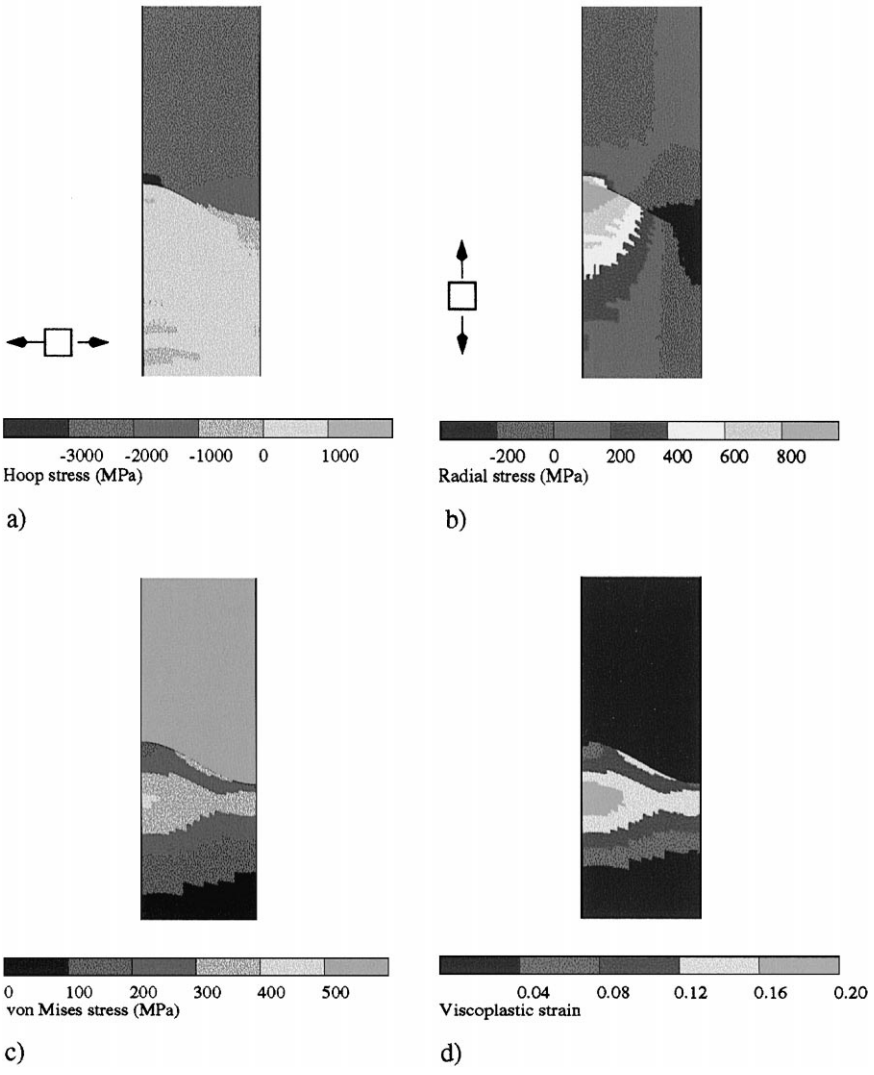

Fig. 8. Distribution of the stresses and viscoplastic strain in the local structure: (a) hoop stress; (b) radial stress; (c) von Mises stress; (d) viscoplastic strain.

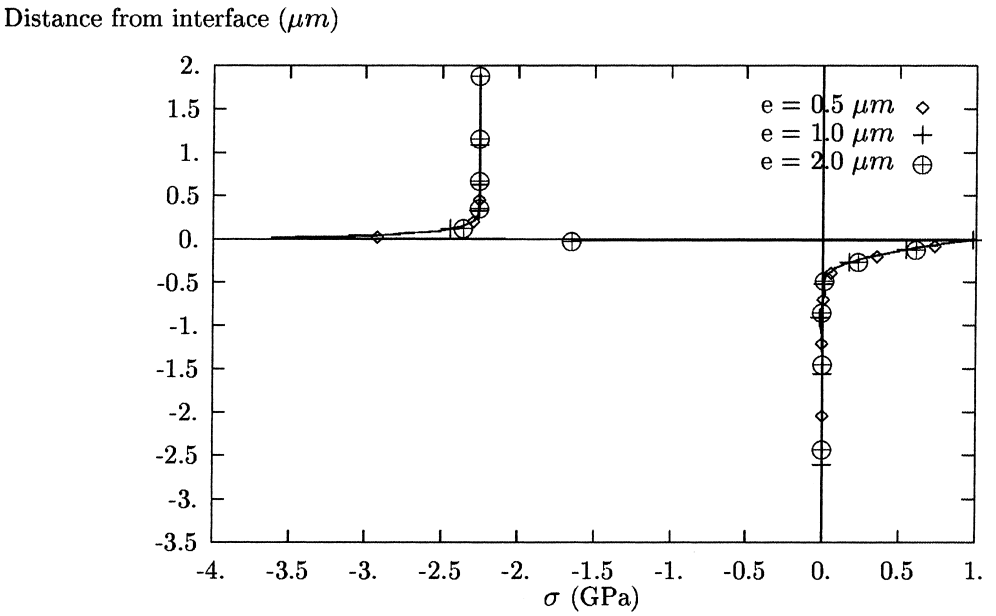

Fig. 9. Variation of the hoop stress along the axis AB of an undulation of the metal–oxide interface, with various oxide thicknesses (undulation amplitude 0.1 μm).

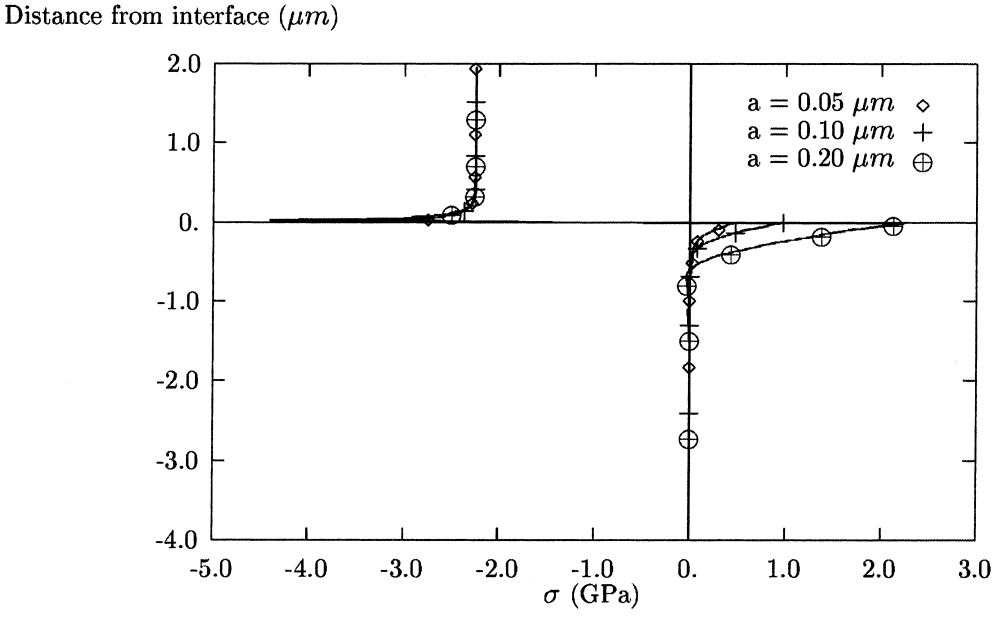

Fig. 10. Variation of the hoop stress along the axis AB of an undulation of the metal–oxide interface, with various undulation amplitude (oxide thickness 2 μm).

axial stresses remain strongly compressive in the oxide but the radial stress is now compressive too. The evolution of the stress state around the undulation is described and summarized in Fig. 13.

5. Conclusion

Two types of computations have been performed in this paper to evaluate the stresses and strains in the met-

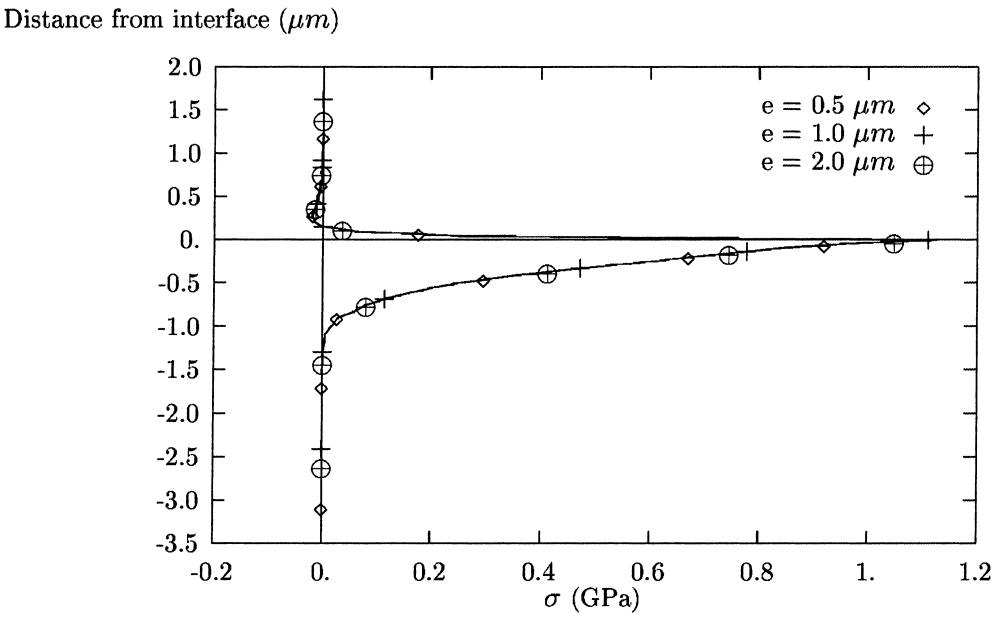

Fig. 11. Variation of the radial stress along the axis AB of an undulation of the metal–oxide interface, with various oxide thickness (undulation amplitude 0.1 μm).

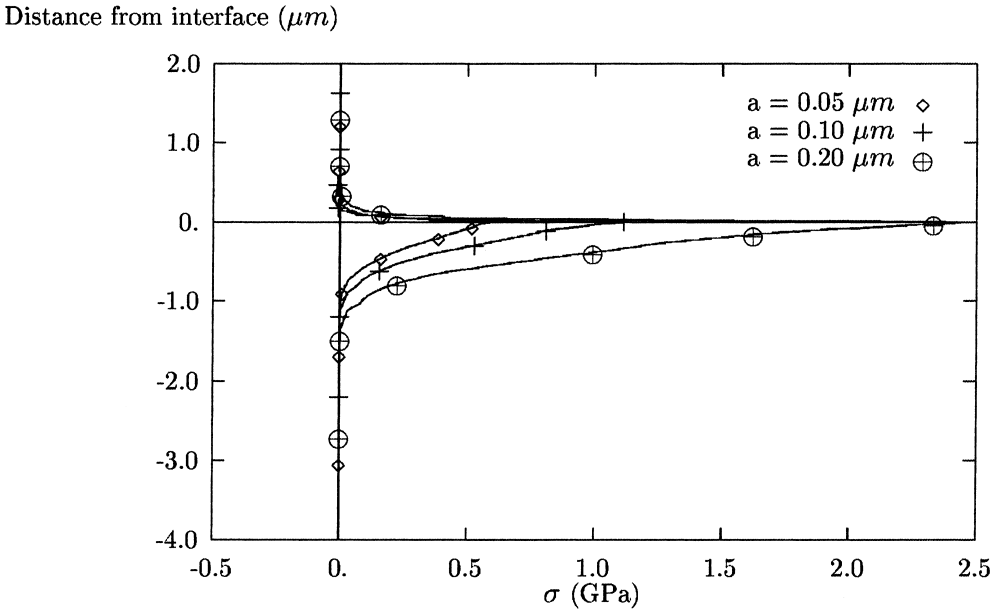

Fig. 12. Variation of the radial stress along the axis AB of an undulation of the metal–oxide interface, with various undulation amplitude (oxide thickness 2 μm).

al and the oxide near the interface during Zircaloy-4 oxidation. The transformation of a volume of matter from metal to oxide has been associated with a highly anisotropic volumic expansion (linear phase transformation dilatation equals 0.005 in the direction parallel to the interface and 0.54 in the normal direction). Through a global modelling, on a 1D geometry, the computed stresses are in good agreement with measured stresses.

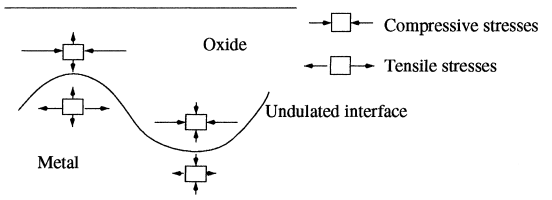

Fig. 13. Schematic distribution of stresses around the undulated interface.

The model evidences a very weak radial stress (about 1 MPa at the metal–oxide interface) and a discontinuous hoop stress with a strong compression in the oxide (about 2 GPa) and weak tensile stresses in the metal. No viscoplastic strain is undergone by the metal with this computation. This kind of computation gives a good idea of the mean stress levels in the oxide scale and in the substrate. But obviously it is not sufficient to describe the possible local stress concentrations leading to observed cracks in the oxide scale.

A local modelling on a 2D geometry has been then performed in order to take into account the interface undulation experimentally observed. Finite element computation has been used to compute the stresses and strains around an undulation of the metal–oxide interface. It has been evidenced that far from the interface, the undulation has no effect on the stress intensities. However, it strongly influences the stresses near the interface.

The level of the hoop and axial stresses is modified depending on whether the curvature is convex or concave. Greater (resp. smaller) compressive stresses correspond to convex (resp. concave) curvature. The radial stress is no longer negligible: significant tensile (resp. compressive) stresses of several hundred MPa arise at the metal–oxide interface in convex (resp. concave) areas. This result shows that cracks could likely appear in the oxide near the convex areas but not in concave ones.

The value of the stresses, independently of the interface undulation, is of course strongly related to the elastic constants and to the value of the phase transformation strain ε_1^{pt}. A better knowledge of the elastic constants of the oxide at the considered temperatures would improve the deflection modelling used to determine ε_1^{pt} and thus will lead to computed values of stresses probably closer to real values.

The results of the local modelling emphasize the role of the undulated geometry of the metal-oxide interface. It appears that two aspects of the oxidation mechanisms are linked through these results. On one hand, since the diffusion coefficient depends on the hydrostatic stress [5], it will be different in two distinct areas of the oxide scale, depending on whether the local hydrostatic stress is high or low, that is depending on the local curvature of the metal–oxide interface. On the other hand the local curvature is related to the local oxide thickness: a convex interface corresponds to a small oxide thickness, i.e. to an area where the oxidation rate is large. Future work will then focus on coupled computation, integrating both diffusion and mechanical aspects.

Acknowledgements

The authors gratefully acknowledge H. Robin for his contribution to the global analysis presented in Section 3 in the framework of a research project at Ecole des Mines de Paris in 1994. This work is a part of the Ph.D. Thesis of M. Parise, at CEA/ Grenoble, financially supported by Electricite de France and Framatome.

Appendix A

Some analytical calculation is needed to obtain the compliance moduli tensor of the textured oxide, when one knows the compliance tensor of monocrystalline monoclinic zirconia. The method used for that purpose is detailed in Ref. [19]. According to the notations of Fig. 1, the grains are oriented so that the (Ox_1, Ox_2) plane of the crystallophysic frame is approximately equal to the metal–oxide interface. Let $S(Ox_1^0, Ox_2^0, Ox_3^0)$ be the reference frame linked to the sample. Let A be the matrix from S to P; A is the matrix of a rotation of an angle α around the Ox_3 (or Ox_3^0) axis. The elastic constants of a monoclinic monocrystal expressed in the P frame C_{ijkl} are linked to their values in the S frame C^0_{pqmn} by the relations

$$C^0_{ijkl} = A_{ip}A_{jq}A_{km}A_{ln}C_{pqmn}, \tag{A.1}$$

$$S^0_{ijkl} = A_{ip}A_{jq}A_{km}A_{ln}S_{pqmn}. \tag{A.2}$$

The values of the elastic constants for the transverse isotropic material are obtained by computing the mean values of these coefficients with α ranking from 0 to 2π: Voigt's hypothesis (uniform strains) gives the result in Eq. (A.3) and Reuss' hypothesis (uniform stresses) leads to Eq. (A.4):

$$C^0_{ijkl} = \frac{1}{2\pi}\int_0^{2\pi} A_{ip}A_{jq}A_{km}A_{ln}C_{pqmn}\ \mathrm{d}\alpha, \tag{A.3}$$

$$S^0_{ijkl} = \frac{1}{2\pi}\int_0^{2\pi} A_{ip}A_{jq}A_{km}A_{ln}S_{pqmn}\ \mathrm{d}\alpha. \tag{A.4}$$

Elementary mathematics allow us to find the bounds of either the moduli or the compliance tensor.

$$C^{V}(\mathrm{GPa}) = \begin{bmatrix} 395 & 141 & 97 & 0 & 0 & 0 \\ 141 & 395 & 97 & 0 & 0 & 0 \\ 97 & 97 & 240 & 0 & 0 & 0 \\ 0 & 0 & 0 & 88.9 & 0 & 0 \\ 0 & 0 & 0 & 0 & 88.9 & 0 \\ 0 & 0 & 0 & 0 & 0 & 127 \end{bmatrix},$$

$$S^{V}(\mathrm{GPa}^{-1}) = \begin{bmatrix} 0.00306 & -0.00088 & -0.00088 & 0 & 0 & 0 \\ -0.00088 & 0.00306 & -0.00088 & 0 & 0 & 0 \\ -0.00088 & -0.00088 & 0.00488 & 0 & 0 & 0 \\ 0 & 0 & 0 & 0.0112 & 0 & 0 \\ 0 & 0 & 0 & 0 & 0.0112 & 0 \\ 0 & 0 & 0 & 0 & 0 & 0.0079 \end{bmatrix},$$

$$C^{R}(\mathrm{GPa}) = \begin{bmatrix} 375 & 156 & 94 & 0 & 0 & 0 \\ 156 & 375 & 94 & 0 & 0 & 0 \\ 94 & 94 & 219 & 0 & 0 & 0 \\ 0 & 0 & 0 & 75 & 0 & 0 \\ 0 & 0 & 0 & 0 & 75 & 0 \\ 0 & 0 & 0 & 0 & 0 & 109 \end{bmatrix},$$

$$S^{R}(\mathrm{GPa}^{-1}) = \begin{bmatrix} 0.0034 & -0.000118 & -0.000118 & 0 & 0 & 0 \\ -0.000118 & 0.0034 & -0.000118 & 0 & 0 & 0 \\ -0.000118 & -0.000118 & 0.00537 & 0 & 0 & 0 \\ 0 & 0 & 0 & 0.0134 & 0 & 0 \\ 0 & 0 & 0 & 0 & 0.0134 & 0 \\ 0 & 0 & 0 & 0 & 0 & 0.0092 \end{bmatrix}.$$

The superscripts R and V refer to the Reuss and Voigt's method, respectively.

References

[1] D.H. Bradhurst, P.M. Heuer, J. Nucl. Mater. 3 (1970) 35.
[2] N.B. Pilling, R.E. Bedworth, J. Inst. Met. 29 (1923) 529.
[3] H.L. Bernstein, Metall. Trans. A 18A (1987) 975.
[4] E.M. Levin, H.F. McMurdie, Phase Diagrams for Ceramists, American Ceramic Society, Westerville, OH, 1975.
[5] C.C. Dollins, M. Jursich, J. Nucl. Mater. 113 (1983) 19.
[6] H.E. Evans, D.J. Norfolk, T. Swan, J. Electrochem. Soc. 125 (1978) 180.
[7] C. Roy, G. David, J. Nucl. Mater. 37 (1970) 71.
[8] F. Antoni-Le Guyadec, PhD dissertation, Institut national Polytechnique de Grenoble (1989).
[9] J.L. Béchade, P. Goudeau, M. Bessiere, P. Yvon, Proceedings of ICRS-5, Linköping, Sweden, 16–18 June 1997.
[10] J. Lemaitre, J.L. Chaboche, Mécanique des matériaux solides, Dunod Bordas, Paris, 1988.
[11] P. Pilvin, in: P. Delobelle, C. Lexcellant, C. Oytana (Eds.), Proceedings of MECAMAT International seminar on Inelastic Behaviour of Solids, 1988.
[12] P. Delobelle, P. Robinet, J. Phys. (Paris) III 8 (1994) 1347.
[13] M.V. Nevitt, S.K. Chan, J.Z. Liu, M.H. Grimsditch, Y. Fang, Physica B 150 (1988) 230.
[14] M. Parise, PhD dissertation, Ecole des Mines de Paris (1996).
[15] J.L. Béchade, J. Godlewski, Proceedings of 11th International symposium on Zirconium in the Nuclear Industry, Garmisch-Partenkirchen, 11–14 September 1995.
[16] J.S. Bryner, J. Nucl. Mater. 82 (1979) 84.
[17] F.H. Stott, A. Atkinson, Mater. High Temp. 12 (2/3) (1994) 195.
[18] Z7, User manual (1997).
[19] D. François, A. Pineau, A. Zaoui, Comportement mécanique des matériaux, Hermes, Paris, 1991.